LETTER

Radiative heat transfer in the extreme near field

Kyeongtae Kim[1]†*, Bai Song[1]*, Víctor Fernández-Hurtado[2]*, Woochul Lee[1], Wonho Jeong[1], Longji Cui[1], Dakotah Thompson[1], Johannes Feist[2], M. T. Homer Reid[3], Francisco J. García-Vidal[2,4], Juan Carlos Cuevas[2], Edgar Meyhofer[1] & Pramod Reddy[1,5]

Radiative transfer of energy at the nanometre length scale is of great importance to a variety of technologies including heat-assisted magnetic recording[1], near-field thermophotovoltaics[2] and lithography[3]. Although experimental advances have enabled elucidation of near-field radiative heat transfer in gaps as small as 20–30 nanometres (refs 4–6), quantitative analysis in the extreme near field (less than 10 nanometres) has been greatly limited by experimental challenges. Moreover, the results of pioneering measurements[7,8] differed from theoretical predictions by orders of magnitude. Here we use custom-fabricated scanning probes with embedded thermocouples[9,10], in conjunction with new microdevices capable of periodic temperature modulation, to measure radiative heat transfer down to gaps as small as two nanometres. For our experiments we deposited suitably chosen metal or dielectric layers on the scanning probes and microdevices, enabling direct study of extreme near-field radiation between silica–silica, silicon nitride–silicon nitride and gold–gold surfaces to reveal marked, gap-size-dependent enhancements of radiative heat transfer. Furthermore, our state-of-the-art calculations of radiative heat transfer, performed within the theoretical framework of fluctuational electrodynamics, are in excellent agreement with our experimental results, providing unambiguous evidence that confirms the validity of this theory[11–13] for modelling radiative heat transfer in gaps as small as a few nanometres. This work lays the foundations required for the rational design of novel technologies that leverage nanoscale radiative heat transfer.

Radiative heat transfer in the far field[14], that is, at gap sizes larger than Wien's wavelength ($\sim$10 μm at room temperature), is well established. However, near-field radiative heat transfer (NFRHT), where the gap sizes are smaller than Wien's wavelength, remains relatively unexplored[15]. Over the past decade, a series of technical advances have enabled experiments[4–6] for gap sizes as small as 20 nm to study NFRHT and broadly verify the validity of a theoretical framework called fluctuational electrodynamics[11,16–18] for modelling NFRHT. In contrast, recent experiments[7,8] of extreme (e)NFRHT with single-digit nanometre gap sizes ($<$10 nm) between gold (Au) surfaces have questioned the validity of fluctuational electrodynamics and have raised the question of whether additional mechanisms, even of non-radiative origin such as phonon tunnelling[19], could dominate the heat transfer in this regime. In addition, some newer computational eNFRHT studies[20] on dielectrics have suggested that the local form of fluctuational electrodynamics, in which one assumes the dielectric properties of the media to be local in space, is inadequate for modelling eNFRHT. Yet other computations[21] on dielectrics have asserted that such non-local effects are irrelevant even for gap sizes as small as 1 nm. This disagreement is of great concern because understanding eNFRHT is critical for the development of a range of novel technologies[1–3]. Here, we present experimental and computational results that both demonstrate marked increases in heat fluxes in the extreme near field and establish the validity of fluctuational electrodynamics for modelling/predicting eNFRHT for dielectric as well as metal surfaces in gap sizes as small as a few nanometres.

Experimental elucidation of radiative heat transfer across few-nanometre-sized gaps is exceedingly difficult, owing to numerous technical challenges in creating and stably maintaining such gaps while simultaneously measuring minute (pW) heat currents across them. One key innovation used in this work to overcome the technical challenges was to leverage highly sensitive, custom-fabricated probes with embedded Au–Cr thermocouples (Fig. 1a–c), called scanning thermal microscopy (SThM) probes[9]. The SThM probes were fabricated by deposition of multiple metal and dielectric layers to create a nanoscopically small Au–Cr thermocouple at the very end of the tip. Our probes were optimized to have both a high thermal resistance[22] ($R_P \approx 10^6$ K W^{-1}) and stiffness[9] ($>$4 N m^{-1}), and were coated with a desired dielectric (silica (SiO$_2$) or silicon nitride (SiN)) or metal (Au) layer. The resulting probes have tip diameters ranging from 350 nm to 900 nm (for details see Fig. 1b and Supplementary Figs 1–3).

The basic strategy for quantifying NFRHT is to record the tip temperature, via the embedded nanoscale thermocouple, which rises in proportion to the radiative heat flow when the tip is displaced towards a heated substrate. To eliminate conductive and convective heat transfer and to remove any water adsorbed to the surfaces, all measurements were performed in an ultra-high vacuum (UHV) using a modified scanning probe microscope (RHK UHV 7500) housed in an ultra-low-noise facility (see Supplementary Information). In performing the measurements, the substrate is heated to an elevated temperature ($T_S = 425$ K) while the SThM probe, mounted in the scanner of the scanning probe microscope, is connected to a thermal reservoir maintained at a temperature $T_R = 310$ K. The spatial separation between the probe and the substrate is reduced at a constant rate of 0.5 nm s^{-1} from a gap size of 50 nm until probe–substrate contact. During this process the temperature difference between the tip (T_P) and the reservoir (T_R), $\Delta T_P = T_P - T_R$, is monitored (see Supplementary Information) via the embedded thermocouple, while the deflection of the cantilever is concurrently measured optically via an incident laser (Fig. 1a).
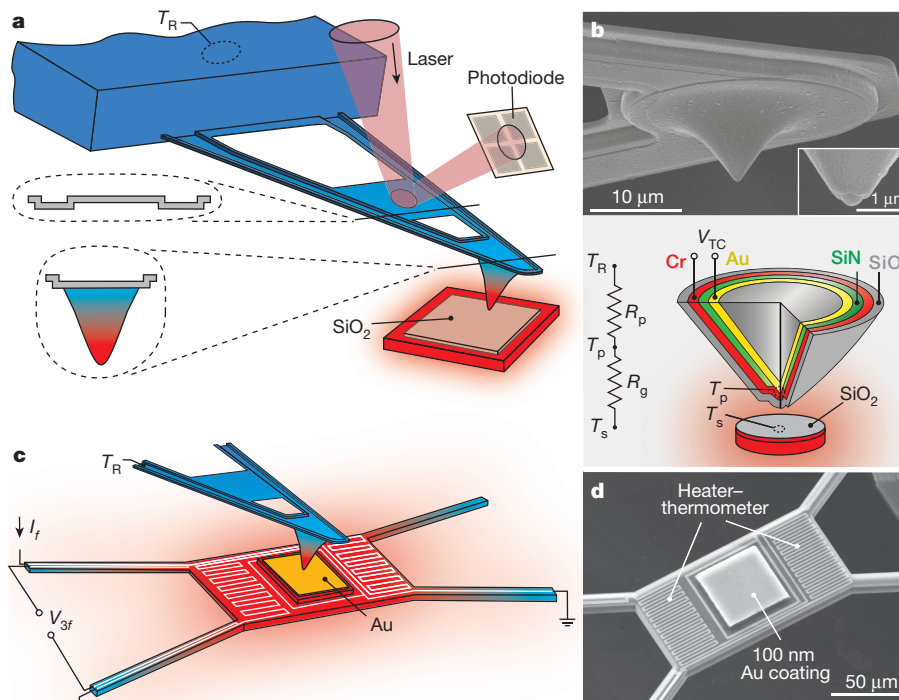
A typical deflection trace for a SiO$_2$-coated tip approaching a SiO$_2$-coated surface is shown in Fig. 2a. From the deflection trace it is apparent that the gap size can be controllably reduced to values as small as $\sim$2 nm, below which the tip rapidly 'snaps' towards the substrate and makes contact (see Supplementary Information). This instability is created by attractive forces between the tip and the substrate that arise owing to Casimir and/or electrostatic forces. Figure 2a shows the simultaneously measured ΔT_P, which represents the sudden increase in temperature that occurs when the tip snaps into the substrate. This rapid increase in tip temperature ($\sim$2 K) upon mechanical contact is due to heat conduction, via the solid–solid contact, from the hot substrate (425 K) to the tip of the SThM probe, the temperature of

Figure 1 | Experimental set-up and SEM images of SThM probes and suspended microdevices. a, Schematic of the experimental set-up, in which an SThM probe is in close proximity to a heated substrate (insets show cross-sections of the SThM probe). The scenario for SiO_2 measurements is shown (the coating on the substrate is replaced with SiN and Au in other experiments). **b**, SEM image (top) of a SThM probe. The inset shows an SEM image of the hemispherical probe tip, which features an embedded Au–Cr thermocouple from which the thermoelectric voltage V_{TC} is measured. The bottom panel illustrates a schematic cross-section for a SiO_2-coated probe used in SiO_2 measurements. For SiN and Au measurements, the outer SiO_2 coating is appropriately substituted as explained in Supplementary Information. A resistance network that describes the thermal resistance of the probe (R_P) and the vacuum gap ($R_g = (G_{eNFRHT})^{-1}$), as well as the temperatures of the substrate (T_S), tip (T_P) and reservoir (T_R) is also shown. **c**, Schematic showing the measurement scheme used for high-resolution eNFRHT measurements of Au–Au. The amplitude of the supplied sinusoidal electric current is I_f, the sinusoidal temperature oscillations at $2f$ are related to the voltage output V_{3f}. **d**, SEM image of the suspended microdevice featuring the central region coated with Au and a serpentine Pt heater–thermometer.

which is ~400 K (heating by the incident laser results in an elevated temperature).

The tight temporal correlation between the mechanical snap-in and the temperature jump of the probe makes it possible to identify tip–substrate contact solely on the basis of temperature signals. In Fig. 2b, the recorded tip temperature is shown as a probe approaches a heated substrate with the laser beam turned off. The recorded temperature signals with and without laser tracking are basically identical (Fig. 2a, b), except that the magnitude of the jump reflects the tip–substrate temperature difference with and without laser excitation. Thus, mechanical contact can be readily detected from the robust temperature jump without laser excitation, thereby avoiding probe heating and laser interference effects. Therefore, we performed all experiments by first estimating the snap-in distance using the optical scheme and subsequently turning the laser off to perform eNFRHT measurements (see Supplementary Information for the measurement of gap size and snap-in distance).

To determine the gap (d)-dependent near-field radiative conductance (G_{eNFRHT}), we measured ΔT_P and directly estimated G_{eNFRHT} from $G_{eNFRHT}(d) = \Delta T_P / [R_P(T_S - T_R - \Delta T_P)]$, where R_P is the thermal resistance of the probe, which was experimentally determined as described in Supplementary Information (Supplementary Fig. 7) to be $1.6 \times 10^6 \, K \, W^{-1}$ and $1.3 \times 10^6 \, K \, W^{-1}$ for the SiO_2- and SiN-coated probes, respectively. The measured conductance of the gaps for SiO_2 and SiN surfaces is shown in Fig. 3a and b, respectively. It can be seen that G_{eNFRHT} increases monotonically until the probe snaps into contact (gap size at snap-in is ~2 nm for both SiO_2 and SiN measurements; see Supplementary Information and Supplementary Fig. 6). Furthermore, it can be seen that the eNFRHT is larger for experiments performed with SiO_2. These measurements represent the first observation of eNFRHT in single-digit nanometre-sized gaps between dielectric surfaces. We compared these results to our computational predictions based on fluctuational electrodynamics, assuming local-dielectric properties (see details later), and found very good agreement (blue lines in Fig. 3a, b).

The remarkable agreement between eNFRHT measurements and computational predictions raises important questions with regards to recent experiments[7] investigating eNFRHT between Au surfaces, which suggested strong disagreements (~500-fold) between predictions of fluctuational electrodynamics and the results of experiments. One may wonder if the good agreement reported above is unique to eNFRHT between polar dielectric materials. To answer this question unambiguously, we performed additional eNFRHT measurements with Au-coated probes and substrates. The measured conductance in these experiments is shown in Fig. 3c. It can be seen that the measured G_{eNFRHT} with decreasing gap size remains comparable to the noise floor of ~220 pW K^{-1} for Au-coated probes at an applied temperature differential of ~115 K (see Supplementary Information) and is much smaller than that observed for polar dielectrics. These measurements set an upper bound of ~250 pW K^{-1} for G_{eNFRHT} in our Au–Au experiments. This result is particularly surprising because previous studies that used probes with smaller diameters and lower thermal resistances[7,23] ((23–$54) \times 10^3 \, K \, W^{-1}$ and ~$10^6 \, K \, W^{-1}$, implying a lower sensitivity than our probes) reported conductances >40 nW K^{-1}, which are at least two orders of magnitude larger than conductances measured by us and predicted by theory.

To resolve this contradiction we needed to improve the resolution of our conductance measurements by more than an order of magnitude (see Supplementary Information and Supplementary
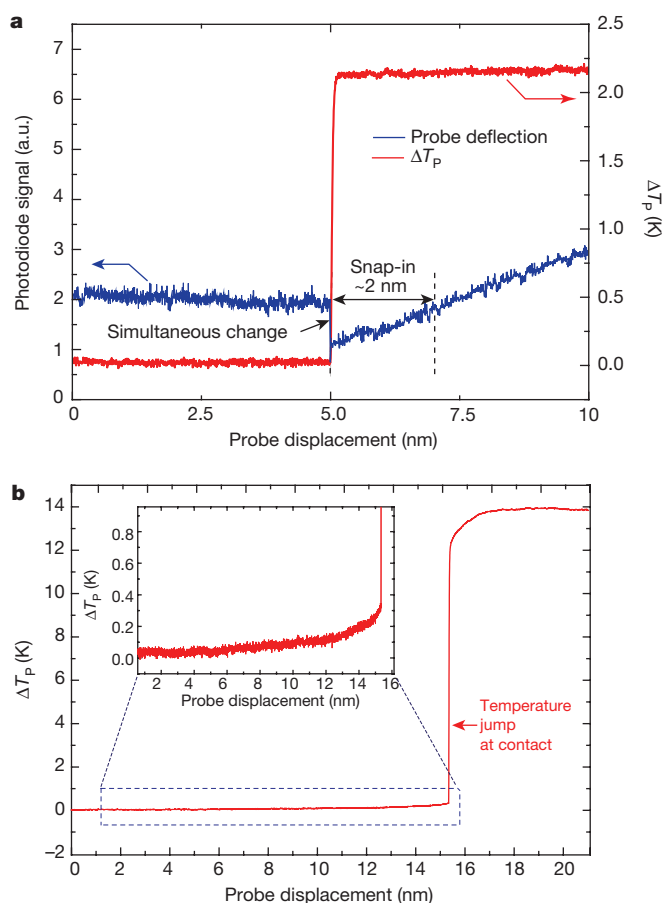
Figure 2 | Detection of mechanical contact from deflection and temperature signals. a, Data from an experiment in which a SiO_2-coated probe at about 400 K (heated by the incident laser) is displaced towards a heated SiO_2 substrate at 425 K. The deflection of the scanning probe (blue), reported in arbitrary units (a.u.), and rise in temperature of probe, ΔT_P (red), are shown. The sudden decrease in the deflection signal due to snap-in coincides with a simultaneous increase in the tip temperature due to conduction of heat from the hot substrate to the cold tip, clearly showing that contact can be readily detected by the large temperature jump. The snap-in distance is seen to be ~2 nm. **b**, Measured ΔT_P when an unheated probe (310 K, laser turned off) is displaced towards the substrate. A sudden increase in the tip temperature is seen when the cold tip contacts the substrate. Inset shows the increase in the tip temperature due to eNFRHT.

Fig. 8 for details). This was accomplished by using a new microdevice (see Fig. 1c, d and Supplementary Figs 4, 5, 9, 10 for details of device fabrication and characterization) that features a suspended island whose temperature can be readily modulated at $f = 18$ Hz (see Supplementary Information). Sinusoidal electric currents (9 Hz) supplied to the embedded electrical heater resulted in sinusoidal temperature oscillations at the second harmonic with amplitude ($\Delta T_{S, f = 18\,Hz}$) that was accurately measured using a lock-in technique[6,24] (see Supplementary Information). To characterize eNFRHT, we positioned a Au-coated SThM probe (30 nm Au thickness) in close proximity to the surface of the microfabricated device, which features a suspended region that is $50\,\mu m \times 50\,\mu m$ large and was coated with 100 nm of Au. The amplitude of temperature modulation of the probe ($\Delta T_{P, f = 18\,Hz}$), due to eNFRHT, was measured at various gap sizes (see Supplementary Information) in a bandwidth of 0.78 mHz. Given the low noise in this bandwidth it was possible to resolve temperature changes as small as ~20 μK, which corresponds to a conductance noise floor of ~6 pW K^{-1}, when $\Delta T_{S, f = 18\,Hz}$ is 5 K (see Supplementary Information section 7 for details of the noise characterization). The measured $\Delta T_{P, f = 18\,Hz}$ values were

used to estimate G_{eNFRHT} (Fig. 3d) via: $G_{eNFRHT}(d) = \Delta T_{P, f = 18\,Hz}/[R_{P,Au}(\Delta T_{S, f = 18\,Hz} - \Delta T_{P f = 18\,Hz})]$, where $R_{P,Au} = 0.7 \times 10^6$ K W^{-1} is the thermal resistance of the Au-coated probe (see Supplementary Information and Supplementary Fig. 7). The smallest gap size at which measurements could be accomplished is ~3 nm and is limited by both snap-in and deflections of the microdevice due to periodic thermal expansion resulting from bimaterial effects (see Supplementary Fig. 11). The measured G_{eNFRHT} (Fig. 3d) is indeed much smaller than that obtained with SiO_2 (Fig. 3a) and SiN (Fig. 3b) films. In contrast to previous experiments[7], our measured G_{eNFRHT} for Au–Au surfaces is in excellent agreement with the predictions of fluctuational electrodynamics (solid line in Fig. 3d).

To obtain insight into our experimental results, we used a fluctuating-surface-current formulation of the radiative heat transfer problem[13,25] combined with the boundary element method, as implemented by us in the SCUFF-EM solver[26]. This allows NFRHT calculations between bodies of arbitrary shape and provides numerically exact results within the framework of fluctuational electrodynamics in the local approximation[13,25]. For our calculations, we characterized the dielectric function for SiN, whereas the dielectric functions for SiO_2 and Au were taken from previous work (see Supplementary Information section 12 and Supplementary Fig. 12). To simulate our experiments accurately, we considered the tip–substrate geometries shown in the left insets of Fig. 4c, d. Here, the tip has a conical shape and ends in a spherical cap whose radius was obtained from scanning electron microscope (SEM) images of the probes (see Supplementary Figs 1–3). In our simulations, we included sufficiently large areas of the probe's conical part and the substrate such that the results do not depend on their finite size (see Supplementary Information section 14 and Supplementary Fig. 13). To maintain high fidelity to the experimental conditions, we also accounted for the small roughness of our probes by including random Gaussian-correlated noise in the tip profile (Fig. 4c, d). More precisely, the maximum protrusion height on the tip and the correlation length between protrusions were chosen to be 10 nm and 17 nm, respectively, on the basis of the surface characteristics observed in the SEM images (Supplementary Figs 1–3). We investigated the effect of surface roughness by computing G_{eNFRHT} for every material from 15 different tip–substrate ensembles with roughness profiles generated as described earlier. The computational results for the different materials are presented in Fig. 3a, b, d. As pointed out earlier, we indeed find very good agreement between computation and experiment without any adjustable parameters.

To elucidate the underlying physical mechanism and explain the differences in eNFRHT between different material combinations, we computed the spectral conductance (heat conductance per unit of energy) for several gap sizes as shown in Fig. 4a, b for SiO_2 and Au, respectively (see Supplementary Fig. 14 for SiN results). In Fig. 4a, one can see that the dominant contributions to the spectral conductance of SiO_2 come from two narrow energy ranges centred around ~0.06 eV and ~0.14 eV, which correspond to the energies of the transverse optical phonons of SiO_2. This strongly suggests that for SiO_2, eNFRHT is dominated by surface phonon polaritons (SPhPs), as previously found for larger gaps[6,27,28]. In turn, this explains the marked decrease in heat transfer as the gap size increases, which is a consequence of the rapid decrease in the number of available surface electromagnetic modes for radiation to tunnel across the vacuum gap. In contrast, eNFRHT for Au exhibits a rather broad spectral conductance that decays more slowly with gap size (Fig. 4b). This slow decay is reminiscent of the situation encountered in a plate–plate geometry[29] where NFRHT is dominated by frustrated internal reflection modes, that is, by modes that are evanescent in the vacuum gap but are propagating inside the Au tip and substrate whose contribution saturates for gaps below the skin depth[29], which for Au is around 25 nm. This naturally explains the weaker dependence of eNFRHT on gap size observed in our Au–Au measurements. The fundamental difference in eNFRHT between dielectrics and metals is also apparent from the computed Poynting-flux
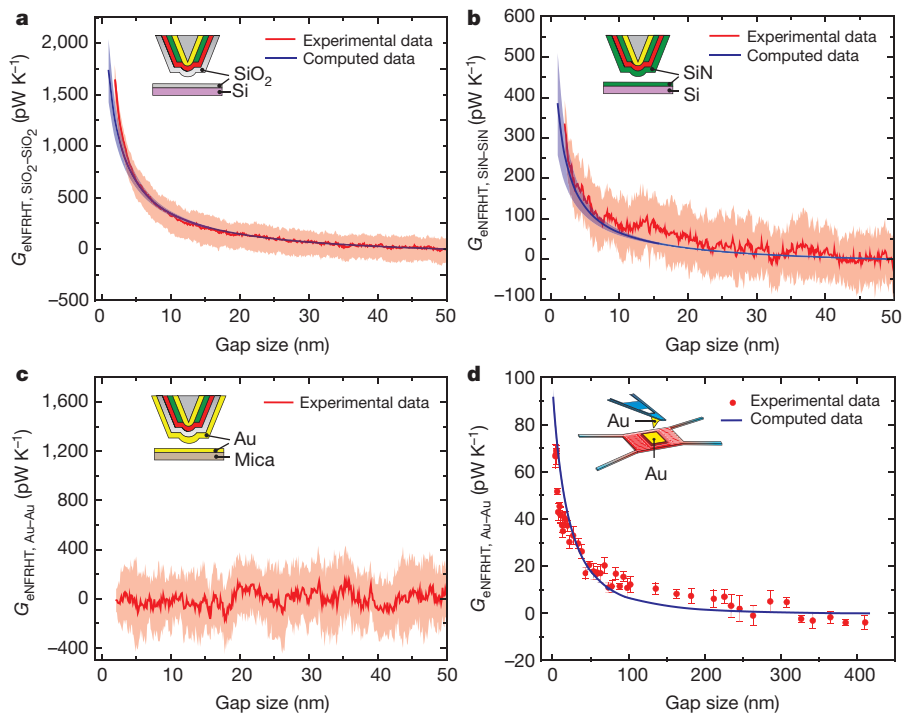
Figure 3 | Measured extreme near-field thermal conductances for dielectric and metal surfaces. a, Measured near-field radiative conductance between a SiO$_2$-coated probe (310 K) and a SiO$_2$ substrate at 425 K. The red solid line shows the average conductance from 15 independent measurements, the light red band represents the standard deviation. The blue solid line shows the average of the computed radiative conductance for 15 different tips with stochastically chosen roughness profiles (root-mean-squared roughness of ~10 nm) and a tip diameter (450 nm) obtained from SEM images of the probe.

The blue shaded region represents the standard deviation in the calculated data. **b**, **c**, Same as **a**, but for SiN–SiN and Au–Au, respectively. The tip diameter is 350 nm for the SiN-coated tip. Computed results are not included for Au–Au. **d**, Near-field conductance from experiments with a Au-coated probe and a suspended microdevice. Red dots represent the average from 10 different measurements (temperature periodically modulated at 18 Hz); the error bars represent the standard deviation. The blue solid line represents the computed conductance (tip diameter is 900 nm).
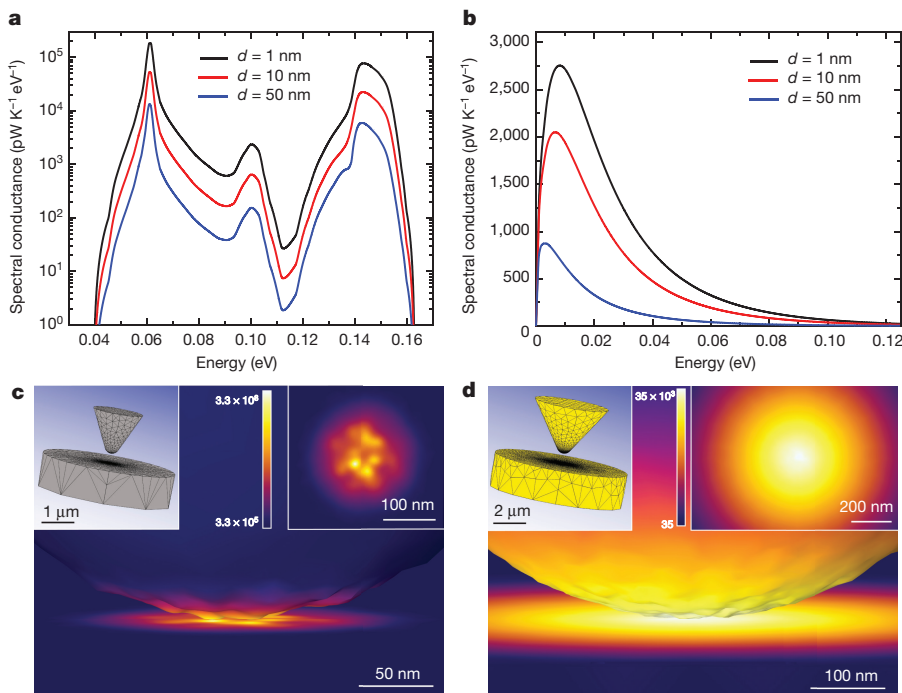
Figure 4 | Spectral conductance and spatial distribution of the Poynting flux. a, Spectral conductance as a function of energy for a SiO$_2$ tip–substrate geometry for three different gap sizes. The tip diameter is 450 nm, and the reservoir temperatures are 310 K for the tip and 425 K for the substrate. Notice the logarithmic scale in the vertical axis. **b**, Same as **a**, but for Au. In this case, the tip radius is 450 nm, and the tip and substrate temperatures are 300 K and 301 K, respectively. **c**, Surface-contour plot showing the spatial distribution of the Poynting-flux pattern on the

surface of the bodies for the SiO$_2$ tip–substrate geometry corresponding to that in **a** with a gap of 1 nm. The colour scale is in units of W (K eV m^2)$^{-1}$ and the plot was computed at an energy of 61 meV, which corresponds to the maximum of the spectral conductance. The right inset shows the corresponding surface heat flux on the substrate; the left inset displays the whole tip–substrate geometry simulated, including the mesh used in the calculations. **d**, Same as **c**, but for Au. In this case the surface-contour plot was computed at 9 meV, the maximum of the spectral conductance.

patterns on the surfaces (Fig. 4c, d), which show that eNFRHT in the SiO$_2$ case is much more concentrated in the tip apex than it is in the Au case. This difference reflects the fact that in a polar dielectric, such as SiO$_2$, eNFRHT has a very strong distance dependence due to the excitation of SPhPs with a penetration depth comparable to the gap size[6]. Given these differences between metals and dielectrics, it is not surprising that Au–Au eNFRHT is relatively insensitive to small surface roughness (see Supplementary Fig. 15). For this reason, the large differences between our results for Au and those of previous work[7,8], which disagree with the predictions of fluctuational electrodynamics, cannot be attributed to differences in the surface roughness. Our computational results, when compared with our experimental data, provide unambiguous evidence that fluctuational electrodynamics accurately describes eNFRHT.

We note that the results presented here provide the first experimental evidence—to our knowledge—for extremely large enhancements of radiative heat transfer in the extreme near field between both dielectric and metal surfaces. Furthermore, our results establish the fundamental validity of fluctuational electrodynamics in modelling eNFRHT and NFRHT. The technical advances described in this work are key to systematically investigating eNFRHT phenomena in a variety of materials and nanostructures, and provide critical information that complements insights that can be obtained by other near-field techniques[30,31]. Knowledge gained from such studies will be critical to the development of future technologies that leverage nanoscale radiative heat transfer[32].

1. Challener, W. A. *et al.* Heat-assisted magnetic recording by a near-field transducer with efficient optical energy transfer. *Nature Photon.* **3,** 220–224 (2009).
2. Basu, S., Zhang, Z. M. & Fu, C. J. Review of near-field thermal radiation and its application to energy conversion. *Int. J. Energy Res.* **33,** 1203–1232 (2009).
3. Pendry, J. B. Radiative exchange of heat between nanostructures. *J. Phys. Condens. Matter* **11,** 6621–6633 (1999).
4. Shen, S., Narayanaswamy, A. & Chen, G. Surface phonon polaritons mediated energy transfer between nanoscale gaps. *Nano Lett.* **9,** 2909–2913 (2009).
5. Rousseau, E. *et al.* Radiative heat transfer at the nanoscale. *Nature Photon.* **3,** 514–517 (2009).
6. Song, B. *et al.* Enhancement of near-field radiative heat transfer using polar dielectric thin films. *Nature Nanotechnol.* **10,** 253–258 (2015).
7. Kittel, A. *et al.* Near-field heat transfer in a scanning thermal microscope. *Phys. Rev. Lett.* **95,** 224301–224304 (2005).
8. Worbes, L., Hellmann, D. & Kittel, A. Enhanced near-field heat flow of a monolayer dielectric island. *Phys. Rev. Lett.* **110,** 134302 (2013).
9. Kim, K., Jeong, W., Lee, W. & Reddy, P. Ultra-high vacuum scanning thermal microscopy for nanometer resolution quantitative thermometry. *ACS Nano* **6,** 4248–4257 (2012).
10. Lee, W. *et al.* Heat dissipation in atomic-scale junctions. *Nature* **498,** 209–212 (2013).
11. Rytov, S. M. *Theory of Electric Fluctuations and Thermal Radiation* (Air Force Cambrige Research Center, 1953).
12. Joulain, K., Mulet, J.-P., Marquier, F., Carminati, R. & Greffet, J.-J. Surface electromagnetic waves thermally excited: radiative heat transfer, coherence properties and Casimir forces revisited in the near field. *Surf. Sci. Rep.* **57,** 59–112 (2005).
13. Rodriguez, A. W., Reid, M. T. H. & Johnson, S. G. Fluctuating-surface-current formulation of radiative heat transfer: theory and applications. *Phys. Rev. B* **88,** 054305 (2013).
14. Planck, M. & Masius, M. *The Theory of Heat Radiation* (P. Blakiston Son & Co, 1914).
15. Song, B., Fiorino, A., Meyhofer, E. & Reddy, P. Near-field radiative thermal transport: From theory to experiment. *AIP Adv.* **5,** 053503 (2015).
16. Rytov, S. M., Kravtsov, Y. A. & Tatarskii, V. I. *Principles of Statistical Radiophysics* (Springer, 1989).
17. Polder, D. & Hove, M. A. V. Theory of radiative heat transfer between closely spaced bodies. *Phys. Rev. B* **4,** 3303–3314 (1971).
18. Shen, S., Mavrokefalos, A., Sambegoro, P. & Chen, G. Nanoscale thermal radiation between two gold surfaces. *Appl. Phys. Lett.* **100,** 233114 (2012).
19. Altfeder, I., Voevodin, A. A. & Roy, A. K. Vacuum phonon tunneling. *Phys. Rev. Lett.* **105,** 166101 (2010).
20. Singer, F., Ezzahri, Y. & Joulain, K. Near field radiative heat transfer between two nonlocal dielectrics. *J. Quant. Spectrosc. Radiat. Transf.* **154,** 55–62 (2015).
21. Chiloyan, V., Garg, J., Esfarjani, K. & Chen, G. Transition from near-field thermal radiation to phonon heat conduction at sub-nanometre gaps. *Nature Commun.* **6,** 6755 (2015).
22. Kim, K. *et al.* Quantification of thermal and contact resistances of scanning thermal probes. *Appl. Phys. Lett.* **105,** 203107 (2014).
23. Wischnath, U. F., Welker, J., Munzel, M. & Kittel, A. The near-field scanning thermal microscope. *Rev. Sci. Instrum.* **79,** 073708 (2008).
24. Sadat, S., Meyhofer, E. & Reddy, P. Resistance thermometry-based picowatt-resolution heat-flow calorimeter. *Appl. Phys. Lett.* **102,** 163110–163113 (2013).
25. Rodriguez, A. W., Reid, M. T. H. & Johnson, S. G. Fluctuating-surface-current formulation of radiative heat transfer for arbitrary geometries. *Phys. Rev. B* **86,** 220302 (2012).
26. Reid, M. T. H. & Johnson, S. G. Efficient computation of power, force and torque in BEM scattering calculations. *IEEE Trans. Antenn. Propag.* **63,** 3588–3598 (2015).
27. Mulet, J. P., Joulain, K., Carminati, R. & Greffet, J. J. Enhanced radiative heat transfer at nanometric distances. *Microscale Therm. Eng.* **6,** 209–222 (2002).
28. Mulet, J. P., Joulain, K., Carminati, R. & Greffet, J. J. Nanoscale radiative heat transfer between a small particle and a plane surface. *Appl. Phys. Lett.* **78,** 2931–2933 (2001).
29. Chapuis, P. O., Volz, S., Henkel, C., Joulain, K. & Greffet, J. J. Effects of spatial dispersion in near-field radiative heat transfer between two parallel metallic surfaces. *Phys. Rev. B* **77,** 035431 (2008).
30. Jones, A. C. & Raschke, M. B. Thermal infrared near-field spectroscopy. *Nano Lett.* **12,** 1475–1481 (2012).
31. De Wilde, Y. *et al.* Thermal radiation scanning tunnelling microscopy. *Nature* **444,** 740–743 (2006).
32. Otey, C. R., Lau, W. T. & Fan, S. H. Thermal rectification through vacuum. *Phys. Rev. Lett.* **104,** 154301 (2010).

Author Contributions The work was conceived by P.R., E.M., F.J.G.-V. and J.C.C. The experiments were performed by K.K., W.L., L.C. and B.S. under the supervision of E.M. and P.R. The devices were designed, fabricated and characterized by K.K., W.J., D.T. and B.S. Characterization of dielectric properties was performed by B.S. Modelling was performed by V.F.-H., J.F. and B.S. (with inputs from M.T.H.R.) under the supervision of F.J.G.-V. and J.C.C. The manuscript was written by J.C.C., E.M. and P.R. with comments and inputs from all authors.

Author Information Reprints and permissions information is available at www.nature.com/reprints. The authors declare no competing financial interests. Readers are welcome to comment on the online version of the paper. Correspondence and requests for materials should be addressed to J.C.C. (juancarlos.cuevas@uam.es) or E.M. (meyhofer@umich.edu) or P.R. (pramodr@umich.edu).